

Three-Dimensional Needle Shape Reconstruction Using an Array of Fiber Bragg Grating Sensors

Roy J. Roesthuis, *Student Member, IEEE*, Marco Kemp, John J. van den Dobbelaar, and Sarthak Misra, *Member, IEEE*

Abstract—We present a prototype of a flexible nitinol needle ($\phi 1.0$ mm and length 172 mm) integrated with an array of 12 Fiber Bragg Grating (FBG) sensors. These sensors measure the axial strain, which enables the computation of the needle curvature. We reconstruct the three-dimensional (3-D) needle shape from the curvature. Experiments are performed where the needle is deflected in free space. The maximum errors between the experiments and beam theory-based model are 0.20 mm (in-plane deflection with single bend), 0.51 mm (in-plane deflection with double bend), and 1.66 mm (out-of-plane). We also describe kinematics-based and mechanics-based models for predicting the 3-D needle shape during insertion into soft tissue. We perform experiments where the needle is inserted into a soft-tissue simulant, and the 3-D needle shape is reconstructed using the FBG sensors. We compare the reconstructed needle shape to deflection obtained from camera images and our models. The maximum error between the experiments and the camera images is 0.74 mm. The maximum errors between the kinematics-based and mechanics-based models and the camera images are 3.77 mm and 2.20 mm, respectively. This study demonstrates that deflection models and needles integrated with FBG sensors have the potential to be used in combination with clinical imaging modalities in order to enable accurate needle steering.

Index Terms—Fiber Bragg gratings (FBGs), kinematics-based model, mechanics-based model, needle deflection models, shape reconstruction, soft tissue.

I. INTRODUCTION

RECENT studies have demonstrated a significant interest in robotically steering a variety of minimally invasive surgical instruments. Examples of such instruments are catheters, flexible needles, and other (fully actuated) miniaturized manipulators. In order to enable accurate control of such instruments, it is essential to know the three-dimensional (3-D) shape of the instrument. In the case of steering flexible needles through soft tissue, previous research used medical imaging techniques, such

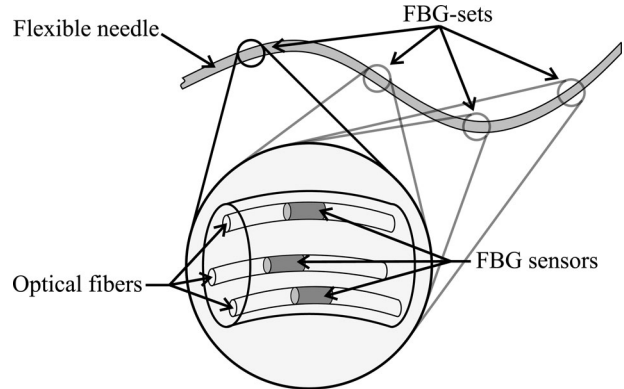


Fig. 1. Fiber Bragg Gratings (FBGs) can be used as sensors to measure the axial strain of a flexible needle. By placing a set of multiple FBGs (in this case three) at a location along the needle shaft, one can determine the needle curvature. In this sketch, an array of four FGB-sets is placed along the length of the needle. Three-dimensional needle shape is reconstructed from needle curvature.

as ultrasound images, X-ray computed tomography (CT) scans and magnetic resonance imaging (MRI), in order to acquire needle shape during insertion [1], [2]. These methods have several drawbacks: Ultrasound can be used in real time but has low tissue contrast. MRI is slow, and hence cannot be used for real-time applications. CT requires high doses of radiation, and can also not be used in real time. More recently, studies have been done in which Fiber Bragg Grating (FBG) sensors have been used to estimate the shape of colonoscopes and needles [3]–[8]. Current technology allows FBG-data to be processed at high speeds (up to 20 kHz), which is fast enough for real-time applications. Moreover, FBG sensors are small in size and therefore, they can be integrated in small diameter surgical instruments. FBGs are also electromagnetically inert, which allows them to be used within a clinical setting without causing electrical interference [7], [9].

FBGs are gratings etched onto an optical fiber, and they have the property to reflect light of a specific wavelength [10]. FBGs are sensitive to changes in mechanical strain or ambient temperature, and these changes cause a shift in the reflected wavelength. Hence, this enables using an FBG as a sensor to measure force, pressure, vibration, or temperature. In previous studies FBG sensors were used to measure axial strain at several locations along the shaft of an instrument [3]–[8]. The curvature was determined from the measured strain, and this curvature was used to reconstruct the shape of the instrument. An example of such an instrument is a needle. Park *et al.* and Henken *et al.* used FBG sensors to determine the shape of a surgical needle which

Manuscript received September 19, 2012; revised December 25, 2012 and May 14, 2013; accepted June 11, 2013. Date of publication July 12, 2013; date of current version April 25, 2014. Recommended by Technical Editor S. Fatikow. This work was supported by the Dutch Technology Foundation STW, which is part of the Netherlands Organisation for Scientific Research (NWO) and partly funded by the Ministry of Economic Affairs, Agriculture and Innovation.

R. J. Roesthuis and S. Misra are with the MIRA—Institute for Biomedical Technology and Technical Medicine, University of Twente, 7500 AE Enschede, The Netherlands (e-mail: r.j.roesthuis@utwente.nl; s.misra@utwente.nl).

M. Kemp is with Océ Technologies B.V., 5914 Venlo, The Netherlands (e-mail: kempmarco@gmail.com).

J. J. van den Dobbelaar is with Delft University of Technology, 2628 CD Delft, The Netherlands (e-mail: j.j.vandendobbelaar@tudelft.nl).

Color versions of one or more of the figures in this paper are available online at <http://ieeexplore.ieee.org>.

Digital Object Identifier 10.1109/TMECH.2013.2269836

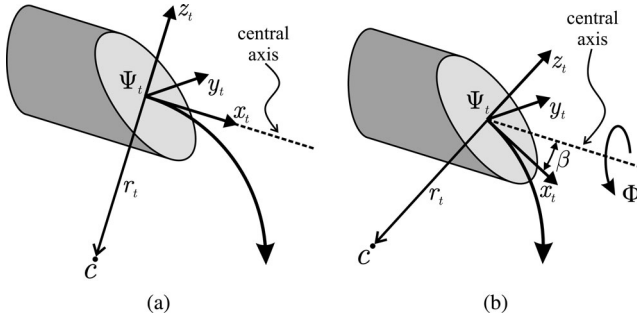


Fig. 2. Coordinate frame (Ψ_t) is rigidly attached to the needle tip. The needle tip describes a circular path with radius (r_t) and center (c). (a) Coordinate frame (Ψ_t) is aligned with the central axis of the needle. This represents the scenario when the cutting of a soft tissue at an angle is not modeled. (b) Cutting of a soft tissue at an angle is modeled by rotating the tip frame by the cut angle (β) around the y_t -axis. Needle rotation is indicated by Φ .

was deflected in free space [7], [8]. Such needles are used in procedures where the goal is to steer the needle to a specific location in the human body (e.g., for diagnosis or therapy) [2]. In order to robotically steer the needle toward a desired target, the position and orientation of the needle during insertion needs to be known. Information about the needle shape can be used as feedback for models which predict the needle path and hence, enable accurate needle steering.

Park *et al.* integrated two FBG-sets (with three FBG sensors for each set) on a surgical needle [7]. They were able to reconstruct the needle shape with a needle tip error of 0.38 mm for deflection applied at the tip of the needle. Henken *et al.* also integrated two FBG-sets (with three FBG sensors for each set) on the inner stylet of a trocar needle [8]. They performed experiments for deflection applied at two locations along the needle shaft, and they achieved a needle tip accuracy of 1.32 mm.

Although Park *et al.* and Henken *et al.* were able to reconstruct the needle shape with high accuracy, they both only considered needle deflection for the planar case (2-D) in free space [7], [8]. The main contribution of this study is that the accuracy of needle tip measurements using FBG sensors is also validated for out-of-plane (3-D) deflections in both free space and a soft-tissue simulant. Further, Park *et al.* and Henken *et al.* both estimated needle curvature by measuring the curvature at two locations along the needle shaft. In this study, three fibers with four FBG sensors (i.e., four sets of FBG sensors) each are used, which enables us to measure needle curvature at four different locations along the needle shaft. These fibers are integrated on a flexible nitinol needle with a bevel tip (see Fig. 1). Such a flexible needle bends much more than a traditional (stiff) needle when inserted into a soft tissue, which is desirable when steering around obstacles. Using this array of four FBG sets, the 3-D needle shape is reconstructed for two different experimental cases for both in-plane and out-of-plane deflections.

First, the needle shape is evaluated for deflection in free space. In the second case, a set of experiments is performed in which the needle is inserted into a soft-tissue simulant (gelatine phantom). Our objective is to combine shape sensing using FBG sensors with models which predict needle deflection. This requires a

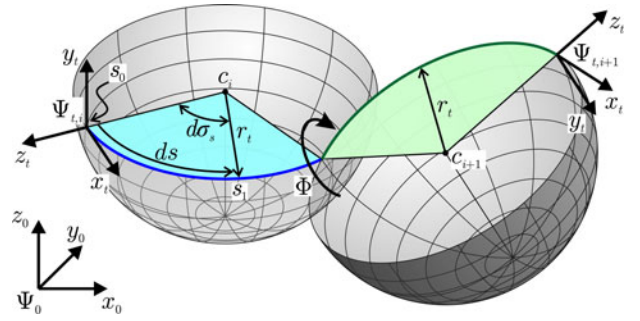


Fig. 3. Needle tip describes a path (blue) along a circle with center at c_i and radius (r_t). After performing needle rotation (Φ), the needle tip follows a circular path (green) described by a circle with center at c_{i+1} .

model which can predict needle deflection in 3-D (i.e., out-of-plane bending). Previously, we have presented a kinematics-based model and a mechanics-based model for predicting needle deflection only for the planar case [11], [12]. In the current study, these models are modified to predict out-of-plane needle deflection. Both deflection models are evaluated for the insertion into gelatine phantoms. The predicted needle shapes and the reconstruction using the FBG sensors are then compared with the deflection determined using camera images. To the best of the authors' knowledge, no other studies have reconstructed the 3-D needle shape for insertion into a soft-tissue simulant using FBG sensors.

The paper is structured as follows. Section II presents the kinematics-based model and mechanics-based model for predicting the 3-D needle shape during insertion into soft tissue. In Section III, the principle of using an array of FBG sensors to reconstruct 3-D needle shape is presented. Section IV describes the experimental setup and fabrication steps of the needle with integrated FBG sensors. The method for calibrating the needle is also presented in this section. The experimental results are presented in Section V, and these include needle shape reconstruction in free space, and within a gelatine phantom. Finally, Section VI concludes, and provides directions for future work.

II. 3-D NEEDLE DEFLECTION MODELS

This section presents two different models for predicting the 3-D deflection of a bevel-tipped flexible needle when inserted into a soft tissue. The first model is a kinematics-based model which considers needle deflection to consist of constant-curvature segments after each needle rotation. The second model is a mechanics-based model which predicts needle deflection based on needle-tissue interaction forces.

A. Kinematics-Based Model

Modeling needle deflection for the planar case using a kinematics-based approach has been done by Webster *et al.* [13]. Needle deflection was described using the nonholonomic kinematics of a unicycle and bicycle. The needle tip was considered to describe a constant-radius path. Furthermore, the tissue is assumed to be stiff enough to ensure that the needle shaft follows the path created by the needle tip. Duindam *et al.* [14] presented

a model to describe the deflection of a bevel-tip flexible needle in 3-D space and used this model to develop a path-planning algorithm. A coordinate frame (Ψ_t) is rigidly attached at the needle tip (Fig. 2(a)). The needle tip moves in the direction of the x_t -axis along a circular path with circle center (c) and radius (r_t). We assume that a bevel-tip cuts tissue at an angle (denoted by cut angle (β)). This is modeled by rotating the tip frame by the cut angle around the y_t -axis (see Fig. 2(b)).

In Fig. 3, a section of the needle path is shown during which rotation (Φ) is performed. The position of the needle tip at a certain instant during insertion depends on the inserted needle length (ds), the number of rotations performed and the angle of each rotation (Φ). In order to describe the needle path, we assumed that initial position and orientation of the needle tip are known. The following homogeneous transformation matrix describes the (initial) position (\mathbf{O}_{t,s_0}^0) and orientation (\mathbf{R}_{t,s_0}^0) of the needle tip at initial location (s_0) with respect to the global coordinate frame (Ψ_0):

$$\mathbf{H}_{t,s_0}^0 = \begin{bmatrix} \mathbf{R}_{t,s_0}^0 & \mathbf{O}_{t,s_0}^0 \\ \mathbf{0}_3^T & 1 \end{bmatrix}. \quad (1)$$

After inserting the needle by ds into the soft tissue, the needle tip is located at s_1 along the circle (see Fig. 3). The position and orientation of the needle tip in the global coordinate frame can be determined by rotating the initial tip frame by an angle ($d\sigma_s$) around circle center (c_i). This angle is related to the bending radius of curvature (r_t) and increase in inserted length (ds) by

$$d\sigma_s = \frac{ds}{r_t}. \quad (2)$$

In order to determine the position of the tip frame at s_1 , first a frame is defined at the circle center (c_i) with an orientation equal to the tip frame at s_0

$$\mathbf{H}_{c_i,s_0}^0 = \begin{bmatrix} \mathbf{R}_{c_i,s_0}^0 & \mathbf{O}_{c_i}^0 \\ \mathbf{0}_3^T & 1 \end{bmatrix} \quad (3)$$

where $\mathbf{O}_{c_i}^0$ is the origin of the circle expressed in the global coordinate frame. The position of the needle tip at s_1 can now be determined by performing a rotation of $d\sigma_s$ around the y_c -axis

$$\mathbf{R}_{t,s_1}^{t,s_0} = \mathbf{R}_{y,c_i}(d\sigma_s) = \begin{bmatrix} \cos(d\sigma_s) & 0 & \sin(d\sigma_s) \\ 0 & 1 & 0 \\ -\sin(d\sigma_s) & 0 & \cos(d\sigma_s) \end{bmatrix}. \quad (4)$$

The needle tip position at s_1 is \mathbf{O}_{t,s_1}^0 , and is calculated as

$$\mathbf{O}_{t,s_1}^0 = \mathbf{H}_{c_i,s_0}^0 \mathbf{t}^{c_i} = \begin{bmatrix} \mathbf{R}_{c_i,s_1}^0 & \mathbf{O}_{c_i}^0 \\ \mathbf{0}_3^T & 1 \end{bmatrix} \mathbf{t}^{c_i} \quad (5)$$

where the rotation (\mathbf{R}_{c_i,s_1}^0) is given by

$$\mathbf{R}_{c_i,s_1}^0 = \mathbf{R}_{t,s_0}^0 \mathbf{R}_{t,s_1}^{t,s_0} \quad (6)$$

and \mathbf{t}^{c_i} equals the position of the needle tip in the circle frame (Ψ_{c_i})

$$\mathbf{t}^{c_i} = [0 \ 0 \ r_t \ 1]^T. \quad (7)$$

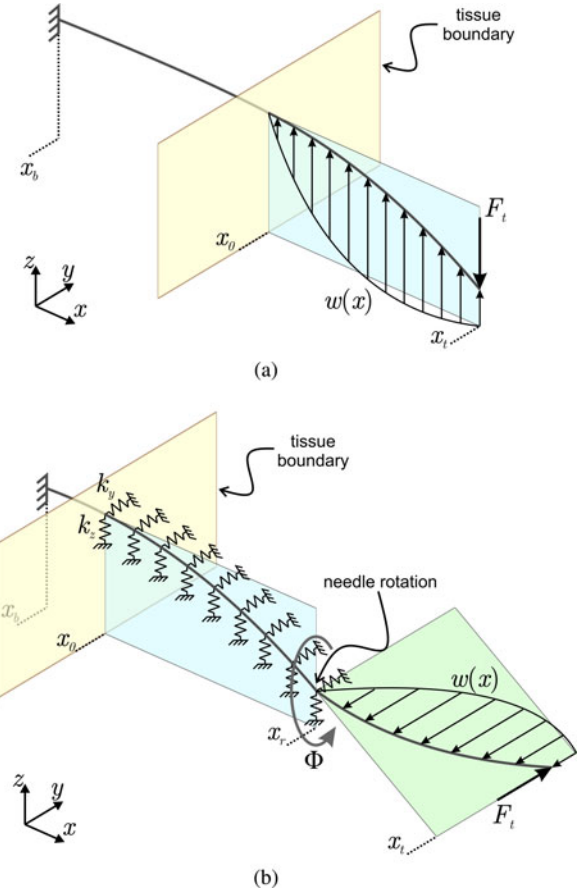


Fig. 4. (a) As the needle is inserted it bends due to tip force (F_t) and distributed load ($w(x)$). (b) Deflected needle shape after a 90° rotation ($\Phi = 90^\circ$) has been performed. The tissue boundary, needle tip position, and the location at which rotation takes place are denoted by x_0 , x_t , and x_r , respectively. The part of the needle prior to rotation ($x_0 \leq x \leq x_r$) is fixed by a series of springs, and tip force and distributed load are applied for the inserted length ($x > x_r$).

Needle rotation is performed by rotating around the central axis of the needle (see Fig. 2(b)). The needle path is predicted by using needle tip position (5) and orientation (6), and the parameters characterizing the needle path (radius (r_t) and cut-angle (β)).

B. Mechanics-Based Model

When a needle is inserted into a soft tissue, it is subjected to needle–tissue interaction forces. These forces have been investigated by the authors in [11] and [15]. A mechanics-based model for predicting the in-plane deflection for a needle which undergoes multiple bends is presented by the authors in [12]. The needle was modeled as a sectioned cantilever beam, and was able to predict complex in-plane bends. The deflected needle shape was evaluated using the Rayleigh–Ritz method, and inputs for the model are a concentrated force at the needle tip and a distributed load along the needle shaft. The tip force is due to cutting of a soft tissue at the needle tip. The distributed load models the support of the needle provided by the surrounding tissue. Deflection with multiple bends is modeled by fixing the

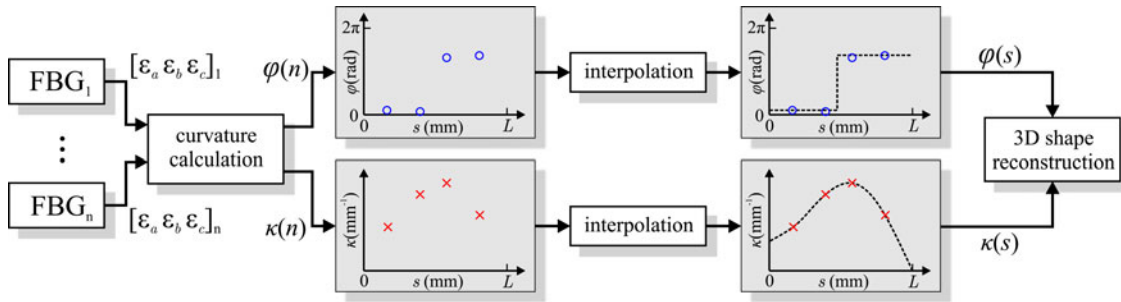


Fig. 5. Flowchart shows the procedure of using an array of Fiber Bragg Grating (FBG) sensors to reconstruct the 3-D needle shape. The needle has a number (n) of FBG-sets along its shaft (FBG_1, \dots, FBG_n), which consist of three FBG sensors each. These are used to measure the axial strain ($\varepsilon_a, \varepsilon_b$ and ε_c) in the needle when it bends, and from this the needle curvature ($\kappa(n)$) and its direction ($\varphi(n)$) are evaluated. Interpolation is performed to compute the continuous curvature ($\kappa(s)$) and its direction ($\varphi(s)$) (position along the needle is denoted by s), and these are used to reconstruct the needle shape.

needle after each rotation with a series of springs, and the next bend is calculated using the tip force and distributed load.

In this study, the mechanics-based model presented in [12] is modified to predict 3-D needle deflection. Since the needle is cylindrical and thus, symmetrical, 3-D deflection can be calculated by separating needle deflection ($v(x)$) for the two planes ($v_{xy}(x)$ and $v_{xz}(x)$) of deflection. The deflection at a position (x) along the needle shaft is given by

$$v(x) = \begin{bmatrix} v_{xy}(x) \\ v_{xz}(x) \end{bmatrix}. \quad (8)$$

The needle is modeled as a cantilever beam, where it is held in a holder at the base (x_b) as shown in Fig. 4. Also, shown are the tip force (F_t) and the distributed load ($w(x)$). Needle insertion is modeled by applying tip force and distributed load each time after a rotation of the needle is performed (see Fig. 4(a)). When needle rotation is performed, the part of the needle prior to rotation ($x_0 \leq x \leq x_r$) is fixed by a series of springs (see Fig. 4(b)). This means that after each needle rotation, the needle is modeled to bend in plane. The direction in which the tip force and distributed load are applied to the needle depends on the rotation angle (Φ) of the needle.

The deflected needle shape is evaluated using the Rayleigh–Ritz method, using tip force and distributed load as inputs. The Rayleigh–Ritz method is a variational method based on the principle of minimum potential energy [16]. The total potential energy (Π) for a mechanical system is expressed as

$$\Pi = U - W \quad (9)$$

where U is the energy stored in the system, and W is the work done by external forces on the system. However, since needle deflection is considered in both planes (xy and xz) separately, the total potential energy can also be expressed independently for both planes (Π_{xy} and Π_{xz}) as

$$\Pi = \begin{bmatrix} \Pi_{xy} \\ \Pi_{xz} \end{bmatrix} = \begin{bmatrix} U_{xy} - W_{xy} \\ U_{xz} - W_{xz} \end{bmatrix} \quad (10)$$

where U_{xy} and U_{xz} is the stored energy and W_{xy} and W_{xz} is the work done by external forces in the xy -plane and xz -plane, respectively.

When needle rotation is not yet performed, the needle is not fixed by springs, and only energy is stored due to transversal

needle bending ($U = U_b$). Using Euler–Bernoulli beam theory [17], the strain energy due to transversal bending (U_b) is found to be

$$U_b = \frac{EI}{2} \int_{x_b}^{x_t} \left(\frac{d^2 v(x)}{dx^2} \right)^2 dx \quad (11)$$

where E and I represent the Young's modulus and second moment of inertia of the needle, respectively. When needle rotation is performed, energy is also stored in the springs, and the total stored energy is now expressed as

$$U = U_b + U_s \quad (12)$$

where U_s is the energy stored in the springs, which is defined as

$$U_s = \sum_{k=1}^m \frac{1}{2} k v(x_k)^2 \quad (13)$$

where $v(x_k)$ is the deflection of the k th spring with respect to the bent shape, and k is the spring constant. The external forces acting on the needle are the tip force and the distributed load. Therefore, the work done by external forces on the system is the sum of work done by the tip force (W_t) and distributed load (W_d)

$$W = W_t + W_d. \quad (14)$$

The work done by the tip force is defined as

$$W_t = F_t v(x_t) \quad (15)$$

where $v(x_t)$ is the needle deflection at the needle tip. The work done by the distributed load is given by

$$W_d = \int_{x_0}^{x_t} w(x) v(x) dx. \quad (16)$$

The Rayleigh–Ritz method requires an assumed displacement function ($v_a(x)$) which satisfies the geometric boundary conditions of the system. A cubic shape function was found to be suitable to approximate the deflected needle shape. Since the needle is divided into a number of elements (n), each element

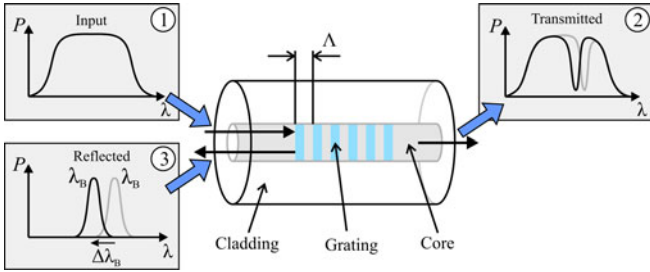


Fig. 6. Schematic of a Fiber Bragg Grating (FBG) sensor. An FBG sensor reflects part of the light which is coupled into the fiber, while light of different wavelength is transmitted. The wavelength of the reflected wavelength is called the Bragg wavelength (λ_B), and depends on the grating period (Λ). The different plots show the power density spectrum (P) of ① the broad-spectrum input light, ② the transmitted light and ③ the reflected light. A change in temperature or applying a mechanical (axial) strain on the fiber results in a shift of the Bragg wavelength ($\Delta\lambda_B$).

(i) is described by its own cubic shape function ($v_{a,i}(x)$)

$$v_a(x) = \begin{cases} v_{a,i}(x), & x_{i-1} \leq x \leq x_i \\ v_{a,i+1}(x), & x_i \leq x \leq x_{i+1} \\ \vdots & \vdots \\ v_{a,n}(x), & x_{n-1} \leq x \leq x_n \end{cases} \quad (17)$$

where $v_{a,i}(x)$ equals

$$v_{a,i}(x) = a_{0,i} + a_{1,i}x + a_{2,i}x^2 + a_{3,i}x^3. \quad (18)$$

The assumed displacement functions (17) are substituted for $v(x)$ in the expressions for stored energy (11)–(13) and work done on the system by external forces (15)–(16). Since 3-D needle deflection is separated into the xy -plane and the xz -plane, the shape function in (17) is defined for both planes independently. This results in the total system potential energy (defined in (9)) being a function of the shape functions and hence, the unknown coefficients

$$\Pi = f(v_i(x)) = f(a_{0,i}, a_{1,i}, a_{2,i}, a_{3,i}). \quad (19)$$

The equilibrium of the system is calculated by taking the partial derivative of the total potential energy with respect to each of the shape functions' unknown coefficients

$$\frac{\partial \Pi}{\partial a_{k,i}} = 0 \quad (20)$$

for $k = 0, 1, 2, 3$ and $i = 1 \dots n$. The unknown coefficients $a_{k,i}$ are calculated by solving the system of equations obtained in (20). The deflected needle shape is calculated by substituting the coefficients back into (17) and (18). The inputs for the model to calculate the deflected needle shape are the tip force, distributed load, and elastic foundation stiffness. In-plane insertion experiments are performed to evaluate these parameters, and this is used to predict deflection for an out-of-plane case (see Section V-B).

III. SHAPE SENSING USING FBG SENSORS

This section discusses the procedure to reconstruct the 3-D needle shape using sets of three FBG sensors each along

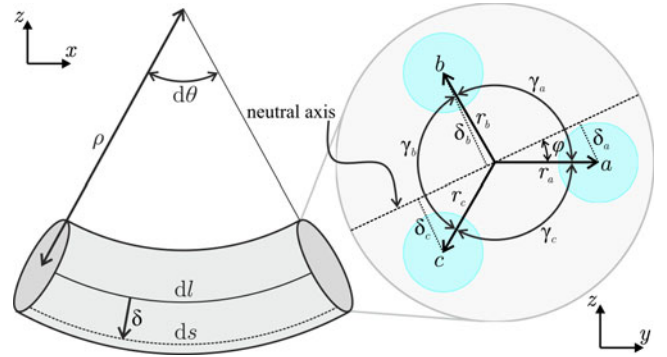


Fig. 7. Section of the needle (of length (dl)) is shown in a bent configuration. A cross section of the needle is shown in the inset. The needle bends about its neutral axis, and the distances from the center of the fibers (a , b , and c) to the neutral axis are denoted by δ_a , δ_b , and δ_c , respectively. The distance from the center of each fiber to the center of the needle are denoted by r_a , r_b , and r_c . The angles between fibers a and b , b and c , c and a are denoted by γ_a , γ_b , and γ_c , respectively.

the length of the needle (see Fig. 5). First, strain is measured from an FBG sensor, and then needle curvature is calculated from multiple sets of three FBG sensors along the needle shaft. Finally, the 3-D needle shape is reconstructed from the curvature.

A. Fiber Bragg Grating Sensor: Theory

An FBG consists of a periodic modulation of the refractive index in the core of a single-mode optical fiber [18]. It has the property to reflect light of a specific wavelength, called the Bragg wavelength (λ_B), which is given by

$$\lambda_B = 2n_e \Lambda \quad (21)$$

where n_e is the effective refractive index of the grating in the fiber core and Λ is the grating period (see Fig. 6). The effective refractive index and the grating period are affected by changes in mechanical strain and temperature and hence, this results in a change in the Bragg wavelength (see Fig. 6). Thus, an FBG can be used as a sensor for either measuring mechanical strain or temperature. The shift in the Bragg wavelength ($\Delta\lambda_B$) due to applied strain (ε_x) and change in temperature (ΔT) is given by [10]

$$\Delta\lambda_B = \lambda_B \left[\underbrace{(1 - p_e)\varepsilon_x}_{\text{strain}} + \underbrace{(\alpha_\Lambda + \alpha_n)\Delta T}_{\text{temperature}} \right] \quad (22)$$

where p_e is a constant which contains the photoelastic contributions, and α_Λ and α_n are the thermal expansion coefficient and the thermo-optic coefficient of the fiber, respectively.

Assuming constant temperature (i.e., $\Delta T = 0$), only the strain applied to the fiber causes a shift in the Bragg wavelength. This means that (22) simplifies to

$$\Delta\lambda_B = \lambda_B (1 - p_e) \varepsilon_x. \quad (23)$$

The axial strain (ε_x) in (23) can be measured by placing a fiber with FBG sensors parallel to the longitudinal axis of the needle. Assuming the needle can be seen as a beam in pure bending

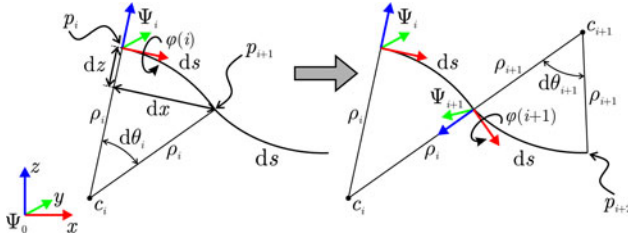


Fig. 8. 3-D needle shape is reconstructed numerically by approximating the needle with elements (ds) of constant curvature.

(see Fig. 7), the following relationship exists between the axial strain in the fiber and the distance (δ) of the fiber to the neutral axis of the needle [17]:

$$\varepsilon_x = \frac{ds - dl}{dl} = \frac{(\rho - \delta) d\theta - \rho d\theta}{\rho d\theta} = -\frac{\delta}{\rho} = -\kappa\delta \quad (24)$$

where κ is the needle curvature, and ρ is its radius of curvature. Substituting (24) into (23) gives an expression which relates the shift in Bragg wavelength to needle curvature

$$\Delta\lambda_B = -\lambda_B (1 - p_e) \kappa\delta. \quad (25)$$

Using (24) and (25), we now determine the needle curvature, and its direction from a set of FBG sensors at a position along the needle shaft.

B. Needle Curvature Calculation

The needle curvature and its direction can be determined by having multiple FBG sensors (in our case three) at the same location along the needle shaft (see Fig. 7). The relationship between the axial strain for a needle in pure bending and the distance from the neutral axis is given in (24). Thus, the following set of equations are derived for the strains at the location of three fibers (denoted by a , b , and c) at a cross section of the needle (see Fig. 7):

$$\begin{aligned} \varepsilon_a &= -\kappa\delta_a = -\kappa r_a \sin(\varphi) + \varepsilon_0 \\ \varepsilon_b &= -\kappa\delta_b = -\kappa r_b \sin(\varphi + \gamma_a) + \varepsilon_0 \\ \varepsilon_c &= -\kappa\delta_c = -\kappa r_c \sin(\varphi + \gamma_a + \gamma_b) + \varepsilon_0 \end{aligned} \quad (26)$$

where φ is the angle between r_a and the neutral axis (see Fig. 7), and indicates the direction of the curvature. A bias may be present in the measured strains due to a change in temperature during the experiment, or due to external forces acting on the needle (e.g., needle–tissue interaction forces during insertion). In (26), this bias is denoted by ε_0 , and is assumed to be equal for each FBG sensor in a set. The position (r_a , r_b , and r_c) and orientation (γ_a , γ_b , and γ_c) of the FBG sensors are assumed to be known and constant (i.e., the neutral axis is always assumed to be at the center of the needle). By solving the set of equations (26), the unknown parameters (needle curvature (κ) and its direction (φ), and the bias (ε_0)) are determined.

C. 3-D Needle Shape Reconstruction

Continuous needle curvature ($\kappa(s)$) and its direction ($\varphi(s)$) are used to reconstruct the 3-D needle shape (see Fig. 5). For

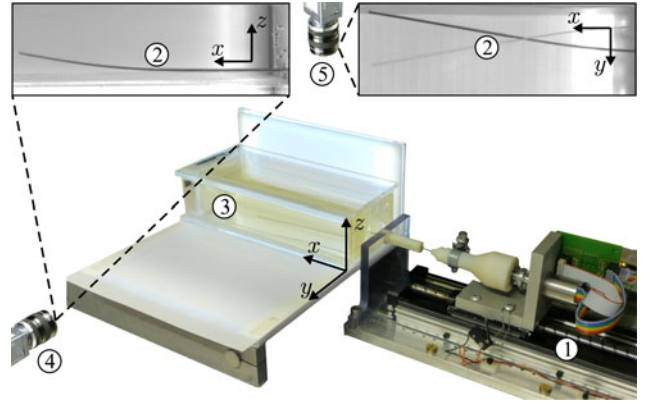


Fig. 9. Experimental setup consists of ① a linear stage which allows insertion of ② the needle into ③ a gelatine phantom, and rotation of the needle during insertion. Two cameras are used to track the needle tip in the ④ xz -plane and the ⑤ xy -plane after needle insertion.

small deflections, the needle shape can be calculated by integrating the curvature ($\frac{d^2v}{dx^2}$) twice. However, for large deflections, this method cannot be used since it does not account for deflection along the longitudinal axis of the needle (i.e., it is assumed that $x = s$). Therefore, the needle shape is reconstructed using a numerical method which approximates the needle with a number (k) of elements (ds) of constant curvature (see Fig. 8). Continuous needle curvature and its direction are first discretized according to the number of elements

$$\begin{aligned} \kappa(s) &\rightarrow \kappa(i) \\ \varphi(s) &\rightarrow \varphi(i) \end{aligned} \quad (27)$$

where $\kappa(i)$ and $\varphi(i)$ are the discretized curvature and its direction of the i th element (where $i = 1, \dots, k$), respectively. The direction in which the needle bends is determined by the direction of needle curvature. The element frames (Ψ_i) are rotated by $\varphi(i)$ around the x -axis such that each element is oriented according to the direction of curvature. Discretized needle curvature ($\kappa(i)$) is used to determine the origin of the frame (p_{i+1}^i) for the next element (see Fig. 8). This requires the angle ($d\theta_i$), which is related to needle curvature ($\kappa(i)$) by

$$d\theta_i = \frac{ds}{\rho_i} = \kappa(i)ds \quad (28)$$

where ρ_i is the radius of curvature. The origin (p_{i+1}^i) of the next frame (Ψ_{i+1}^i), expressed in the current frame (Ψ_i^i) is calculated by

$$\begin{aligned} p_{i+1}^i &= [dx \ 0 \ dz]^T \\ &= [\rho_i \sin(d\theta_i) \ 0 \ -(\rho_i - \rho_i \cos(d\theta_i))]^T. \end{aligned} \quad (29)$$

Finally, a homogeneous transformation (\mathbf{H}_i^0) is performed to calculate the position of the origin in the global coordinate frame (Ψ_0)

$$\begin{bmatrix} p_{i+1}^0 \\ 1 \end{bmatrix} = \mathbf{H}_i^0 \begin{bmatrix} p_{i+1}^i \\ 1 \end{bmatrix} = \begin{bmatrix} \mathbf{R}_i^0 & p_i^0 \\ \mathbf{0}_3^T & 1 \end{bmatrix} \begin{bmatrix} p_{i+1}^i \\ 1 \end{bmatrix} \quad (30)$$

where p_i^0 and \mathbf{R}_i^0 are the position and orientation of the current element frame (Ψ_i) expressed in the global coordinate frame,

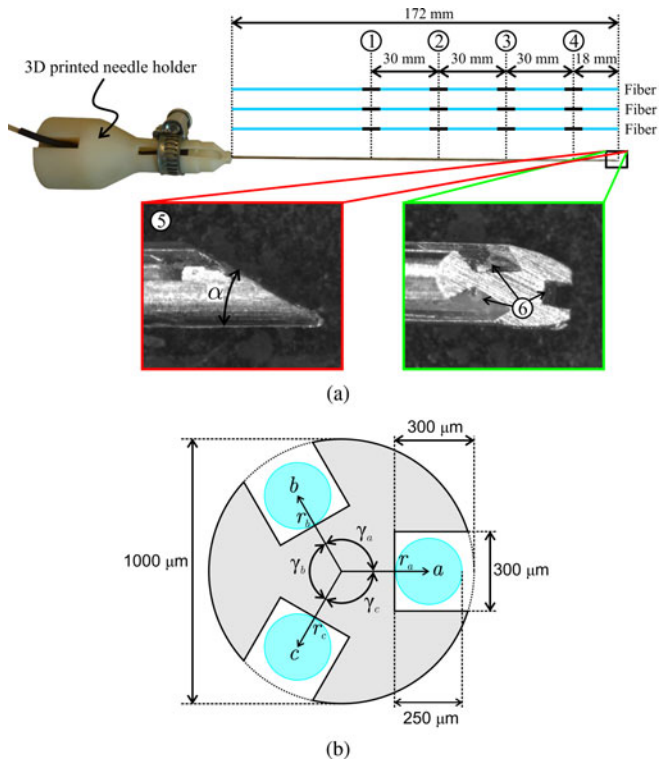


Fig. 10. (a) Photograph of the experimental needle with integrated fibers (FBG-needle). The needle is fixed in a holder which is mounted on the needle insertion device. ①–④ The locations of the four Fiber Bragg Grating-sets (FBG₁, FBG₂, FBG₃ and FBG₄) along the needle shaft. ⑤ Microscopic photograph of the tip with bevel angle ($\alpha = 30^\circ$). ⑥ Top view of the tip. The grooves which hold the fibers are also shown. (b) Cross-sectional view of the needle showing the grooves in which the fibers are glued along the entire length of the needle.

respectively. By repeatedly doing the calculations in (28)–(30) for all elements, the 3-D needle shape is reconstructed.

IV. MATERIALS AND METHODS

This section describes the experimental setup and the needle equipped with FBG sensors (FBG-needle). Experiments to calibrate the position and orientation of the FBG sensors along the needle are also described.

A. Experimental Setup

A setup was designed for needle insertion into a soft tissue [15]. This setup has 2 DOFs: insertion of the needle along its longitudinal axis, and rotation about the same axis (see Fig. 9). Gelatine is used as a soft-tissue simulant. Phantoms are made by dissolving gelatine powder (Dr. Oetker, Bielefeld, Germany) into water, while heating it up to 40 °C. This mixture is then placed in a refrigerator for about 12 h at a temperature of 7 °C to allow the gelatine to stiffen. Insertion experiments are performed immediately after taking the gelatine phantom from the refrigerator. The stiffness of the gelatine phantom depends on the mass ratio between the gelatine powder and water. A percentage of 14.9% gelatine and 85.1% water results in a phantom with a Young's modulus of 35 kPa. The Young's modulus of the phantom is determined by performing a uniaxial compression

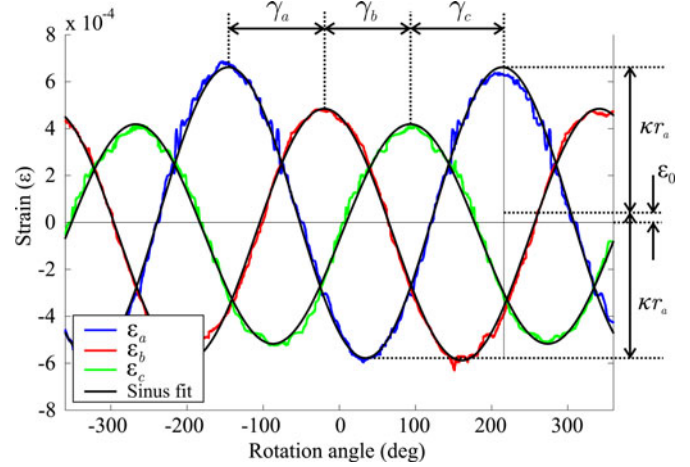


Fig. 11. Calibration experiment is performed to determine the position and orientation for each Fiber Bragg Grating (FBG) sensor. A known curvature (κ) and its direction (φ) are inputs for the experiment. This results in a sinusoidal strain measured by the FBG sensors. A sinusoidal function is fitted to the measured strains, and from this the position (r_* , for * = a, b, c) and orientation (γ_* , for * = a, b, c) of each FBG sensor is determined. The representative plot depicts the strains measured by FBG₁ for a tip deflection of 10 mm ($\Delta y_1 = 10$ mm). The sinusoids fitted to the measured strains are also shown.

test on samples of the phantom using the Anton Paar Physica MCR501 (Anton Paar GmbH, Graz, Austria) rheometer. This value is similar to the elasticity of human breast tissue [19]. Each needle insertion is performed at a different location than the previous insertion, since gelatine is damaged after an insertion. Two charge coupled device (CCD) cameras are mounted at orthogonal angles to determine needle deflection in the xy -plane and xz -plane. A corner-detection algorithm is used to track the needle tip in the recorded videos after needle insertion [15].

B. FBG-Needle Fabrication

A nitinol needle is used for the experiments. Nitinol has a Young's modulus of 75 GPa, which makes it more elastic than traditional steel needles ($E = 200$ GPa). Thus, nitinol is more suitable for needle steering purposes, since it allows for larger curvature bends. A nitinol wire with a length of 172 mm ($\phi 1.0$ mm) is used for the fabrication of the FBG-needle. The needle is shown in Fig. 10(a). Four FBGs are etched into three fibers ($\phi 250 \mu\text{m}$), resulting in a total of 12 FBGs. The last FBG-set (FBG₄) is at 18 mm from the needle tip, while the other FBG-sets are spaced 30 mm from each other. In order to integrate the fibers on the needle, three grooves are milled along the length of the needle at 120° angles from each other (see Fig. 10(b)). The fibers are glued into the grooves using X60 two component adhesive (HBM Germany, Darmstadt, Germany). Finally, a bevel angle of 30° is polished at the needle tip.

The fibers are connected to a Deminsys Pyton interrogator (Technobis, Uitgeest, The Netherlands) which measures the reflected wavelength for each of the 12 FBGs. The measured wavelength is processed at a rate of 100 Hz. The interrogator in turn is connected to a computer via an ethernet cable, and communication is done using a UDP-protocol. The relevant sensor information is retrieved from the UDP-packets using C++.

TABLE I

CALIBRATED VALUES FOR THE POSITION (r_*) AND ORIENTATION (γ_*) FOR EACH FIBER BRAGG GRATING (FBG) SENSOR (* = a, b, c) IN THE FOUR DIFFERENT FBG-SETS (FBG₁, FBG₂, FBG₃, AND FBG₄). MEAN VALUES AND STANDARD DEVIATION (IN BRACKETS) ARE REPORTED BELOW

	FBG ₁		FBG ₂		FBG ₃		FBG ₄	
Fiber	r_* (μm)	γ_* (°)						
a	356 (21)	126.2 (4.8)	395 (22)	123.8 (3.8)	382 (28)	118.7 (2.0)	437 (37)	109.7 (6.6)
b	312 (15)	113.6 (0.6)	307 (29)	117.6 (0.7)	299 (29)	121.8 (1.4)	328 (62)	124.8 (13.8)
c	266 (16)	120.2 (0.8)	299 (24)	118.6 (1.8)	321 (29)	119.4 (3.1)	342 (70)	125.6 (12.5)

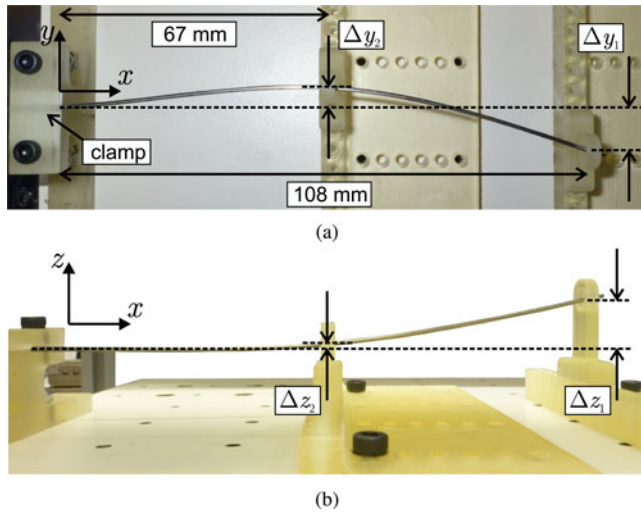


Fig. 12. Experimental setup used for applying free-space needle deflection at two different locations along the needle shaft: Near (6 mm) the needle tip and at 67 mm from the base of the needle. Total needle length is 114 mm. (a) Top view of the setup where deflection in the y -direction is shown (Δy_2 and Δy_1). (b) Side view of the setup where deflection applied in the z -direction (Δz_2 and Δz_1) is shown. Three experimental deflection cases are considered: Case I (in-plane – single bend), Case II (in-plane – double bend), and Case III (out-of-plane).

Postprocessing of the experimental data is done in MATLAB (MathWorks, Inc., Natick, MA, USA).

C. FBG-Needle Calibration

Each FBG sensor measures a strain which is related to needle bending, given by the needle curvature (κ), and its direction (φ). In order to determine the needle curvature from the measured strains, the position (r_a, r_b and r_c) and orientation (γ_a, γ_b and γ_c) of each FBG sensor needs to be known. Due to limited accuracy during the fabrication process of the FBG-needle (e.g., glueing is done manually), the position and orientation of the FBG sensors are not exactly known.

A calibration experiment is performed to determine the position and orientation of each FBG sensor. This is done by applying a known displacement at the tip of the needle, while rotation is applied at the needle base. This rotation causes the direction of curvature to change and hence, results in a sinusoidal strain for each FBG sensor as shown in (26). The strains measured by the three FBG sensors are shown in Fig. 11 for FBG₁. The applied tip deflection for this experiment is 10 mm. A sinus function is fitted to the measured strain. The amplitude of the sinus equals the product of curvature and distance of the fiber from the center of the needle (i.e., κr_*). Using Euler–Bernoulli beam theory, the curvature along the length of the needle is calculated from the applied tip deflection, and this is used to determine the position

TABLE II
ERRORS IN THE RECONSTRUCTED NEEDLE SHAPE USING FIBER BRAGG GRATING (FBG) SENSORS FOR DEFLECTION IN A FREE SPACE (CASES I–III)

Case	Plane	ϵ_s (mm)	$\epsilon_{s,\max}$ (mm)	ϵ_t (mm)
I	xy	0.06 (0.06)	0.20 (0.20)	0.20 (0.21)
II	xy	0.20 (0.05)	0.51 (0.09)	0.38 (0.18)
III	xy	0.30 (0.16)	1.66 (0.57)	1.22 (0.69)
	xz	0.18 (0.08)	0.58 (0.08)	0.46 (0.26)

Mean values and standard deviation (in Brackets) are provided. Overall error (ϵ_s), maximum error ($\epsilon_{s,\max}$), and tip error (ϵ_t) are evaluated. Each experiment is repeated three times.

(r_*) of each FBG sensor. The angles (γ_*) between the fibers are determined from the differences in phase between the measured strains (see Fig. 11). The experiment is performed for different tip deflections (10, 20, and 30 mm), resulting in the positions and orientations of the FBG sensors as listed in Table I. These values are used to calculate needle curvature for the experiments in the next section.

V. RESULTS

This section describes the experiments conducted with the FBG-needle. The needle shape is reconstructed for several experimental cases. These include both in-plane and out-of-plane deflection for free space, and insertion within gelatine phantoms. The kinematics-based and mechanics-based models are also validated with the soft-tissue simulant.

A. Free-Space Deflection

An experimental setup is built to apply deflection at two different locations along the needle shaft (see Fig. 12). The following experimental cases are considered for needle shape reconstruction using FBG sensors in free-space.

- In-plane—single bend: Deflection is applied near the needle tip ($x = 108$ mm) in the y -direction (Δy_1). This results in an in-plane deflection with a single bend. Δy_1 is varied from -25 to $+25$ mm with a resolution of 5 mm.
- In-plane—double bend: Deflection is applied along the needle shaft ($x = 67$ mm) and near the needle tip ($x = 108$ mm) in the y -direction (Δy_2 and Δy_1 , respectively). This results in an in-plane deflection with a double bend. Δy_2 is fixed at -5 mm, while Δy_1 is varied from -5 to $+5$ mm with a resolution of 5 mm.
- Out-of-plane: Deflection is applied along the needle shaft ($x = 67$ mm) and near the needle tip ($x = 108$ mm) in both the y -direction and z -direction (Δy_2 and Δz_2 , and Δy_1 and Δz_1 , respectively). This results in an out-of-plane deflection. Δy_2 and Δz_2 are fixed at -5 and 0 mm, while Δy_1 and Δz_1 are varied from -5 to -10 mm and from $+5$ to $+10$ mm, with a resolution of 5 mm, respectively.

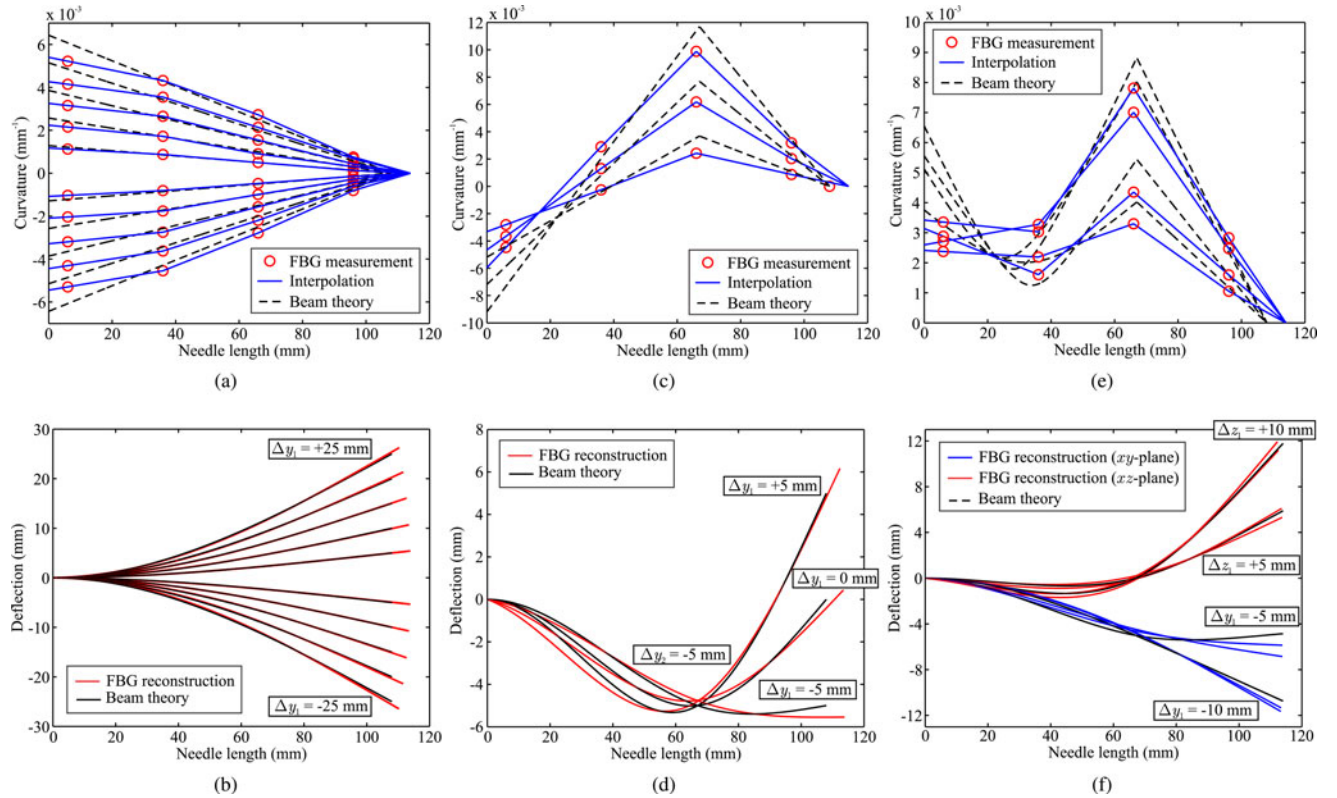


Fig. 13. Needle curvature and deflection for the experimental cases in a free space: (a) and (b) Case I (in-plane—single bend), (c) and (d) Case II (in-plane—double bend) and (e) and (f) Case III (out-of-plane). The discrete curvature values are measured by the Fiber Bragg Grating (FBG) sensors. Linear spline interpolation is used to compute continuous needle curvature. The needle shape is reconstructed using the method presented in Section III-C, and is compared to the theoretical deflection using beam theory. For the purposes of clarity in Case III, deflection is separately shown in the *xy*-plane and *xz*-plane.

Discrete needle curvature is measured by the four FBG-sets, and the results are shown in Fig. 13(a), (c), and (e). Continuous needle curvature is computed using linear spline interpolation, and theoretical curvature is calculated using beam theory. For all deflection cases it is observed that there is a difference in measured needle curvature using FBG sensors, and theoretical curvature near the base of the needle. A cause for this difference may be the assumption of zero needle slope at the needle base, which is used in calculating theoretical needle curvature. Therefore, a nonzero slope at the base of the needle is taken into account for the reconstruction of the deflected needle shape.

Needle deflection is calculated using the method described in Section III-C. The reconstructed needle shapes are compared to theoretical deflection (see Fig. 13(b), (d), and (f)). The errors for the reconstructed needle shape are calculated and provided in Table II. The reconstructed deflection using FBG sensors shows close agreement with Case I and Case II, resulting in maximum errors of 0.20 and 0.51 mm along the needle shaft, respectively. The error at the needle tip is 0.20 mm for Case I and 0.38 mm for Case II. The errors for the out-of-plane experiments (see Case III) are larger than the errors for the in-plane experiments. Maximum errors for Case III along the needle shaft are 1.66 and 0.58 mm, and the error at the needle tip are 1.22 and 0.46 mm for the *xy*-plane and *xz*-plane, respectively.

These results indicate that errors in reconstructed needle shape become larger for complex deflections (i.e., multiple bends and out-of-plane bending). These errors are dependent

on the needle curvature approximation technique. Linear spline interpolation may not be sufficient to approximate needle curvature, as can be seen from the nonlinear curvature for Case III near the needle base (see Fig. 13(e)). Furthermore, we assume that the neutral plane of bending is always at the needle center due to needle symmetry. But due to the grooves in the needle, the needle may bend asymmetrically. Hence, the position of the FBG sensors are not constant during bending and this causes errors in the calculated needle curvature.

B. Needle Insertion into Gelatine Phantoms

The FBG-needle is inserted 115 mm into the gelatine phantom at 10 mm/s. The following experimental cases are considered to evaluate both the needle shape reconstruction using FBG sensors, and also validation of the kinematics- and mechanics-based models.

- IV. In-plane—single bend: The needle is inserted into the gelatine phantom without rotation. This results in an in-plane deflection with a single bend.
- V. In-plane—double bend: The needle is inserted into the gelatine phantom with a 180° rotation at an insertion distance of 35 mm. This results in an in-plane deflection with a double bend.
- VI. Out-of-plane: The needle is inserted into the gelatine phantom with a 90° rotation at an insertion distance of 55 mm. This results in an out-of-plane deflection.

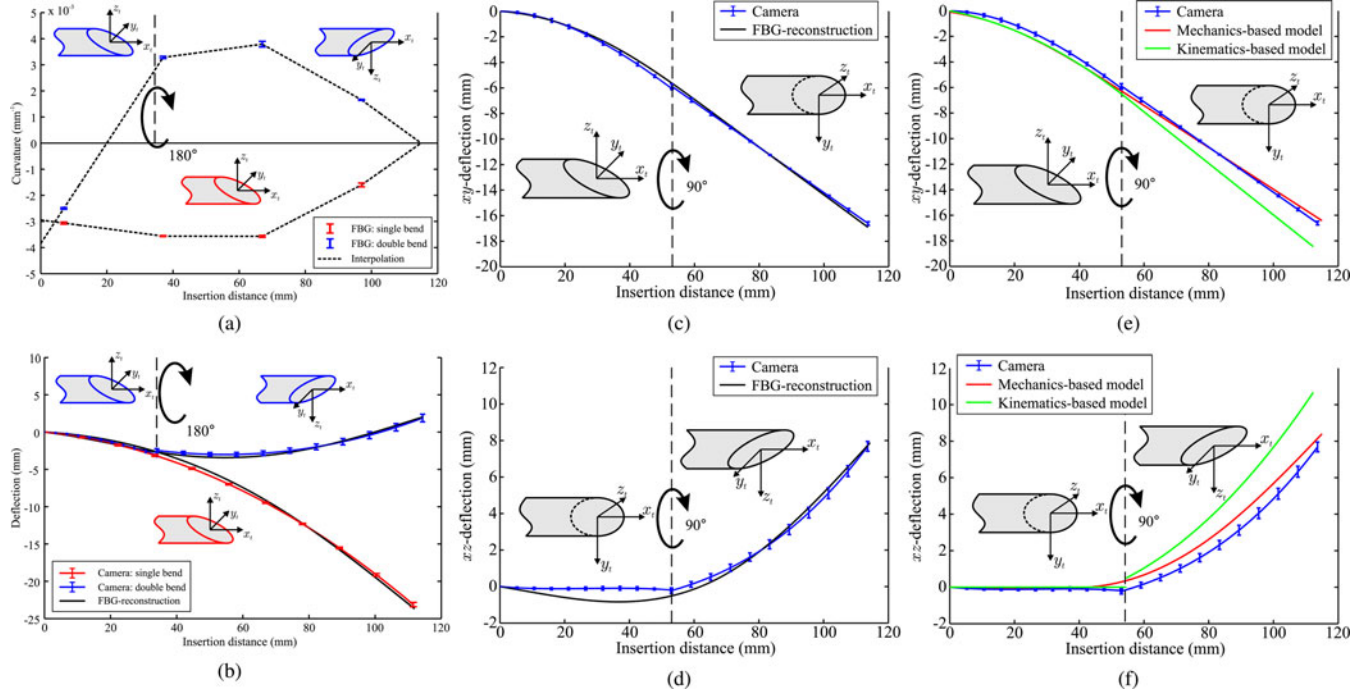


Fig. 14. Results for the needle insertion in gelatine. (a) Measured needle curvature using Fiber Bragg Grating (FBG) sensors and the computed linear spline interpolant are shown for Case IV (in-plane—single bend) and Case V (in-plane—double bend). (b) Reconstructed needle shape using FBG sensors compared with experimental deflection using camera images for Case IV and Case V. (c) and (d) Reconstructed needle shape is compared with experimental deflection for Case VI (out-of-plane) in the xy -plane and xz -plane, respectively. (e) and (f) Predicted needle shape using the kinematics-based and mechanics-based models is compared with experimental deflection for Case VI (out-of-plane) in the xy -plane and xz -plane, respectively. The errors in reconstructed and predicted needle shape are provided in Table III.

The curvature measured by the FBG sensors for Cases IV and V are shown in Fig. 14(a). Linear spline interpolation is used to compute continuous needle curvature from the discrete curvature values measured by the FBG sensors. The curvature is almost constant until FBG_3 , and then the curvature decreases at the needle tip. The curvature for the double bend insertion (see Fig. 14(a)) looks similar to double bend deflection in free space (see Fig. 13(c)). However, as opposed to the deflection in a free space, we do not have a direct method to compare the measured needle curvature with the theoretical curvature.

The reconstructed needle shapes are compared to tip positions that are tracked using a set of CCD cameras [20]. The deflections for Cases IV and V are shown in Fig. 14(b). The resulting deflection for the out-of-plane insertion are shown in Fig. 14(c) and (d) for the xy -plane and xz -plane, respectively. The errors between reconstructed needle shapes using FBG sensors and deflections determined from camera images are presented in Table III. The maximum errors in reconstructed needle shape are 0.57 and 0.53 mm for Cases IV and V, respectively. The maximum errors for Case VI are 0.47 mm in the xy -plane and 0.74 mm in the xz -plane.

The single and double bend experimental deflections (Case IV and Case V, respectively) are used to fit the parameters of both the kinematics-based model and mechanics-based model [12]. The bending radius of curvature r_t is evaluated by fitting a circle to the single bend deflection (see Case IV). The double bend (see Case V) experimental deflection is used to determine the cut-angle (β). Three insertions are performed for both the single and double bend cases. The radius of curvature and cut angle are

calculated to be 366.9 mm ($\sigma = 13.1$ mm) and 2.6° , respectively. These are provided as inputs to the kinematics-based model.

The mechanics-based model requires the tip force F_t and distributed loads ($w(x)$) as inputs. Furthermore, the stiffness K_0 of the elastic foundation also needs to be known. The tip force was determined in a previous study for a $\phi 1$ mm needle and in a gelatine phantom of the same composition [15]. The tip force was found to be 0.40 N. The distributed load is evaluated by fitting the model to experimental deflection data. This fitting is done by minimizing the error between simulated needle deflection and experimental needle deflection for both the single and double bend cases. It is found that a cubic load profile gives the best fit with the experimental deflection [12]. An optimized (minimizing the deflection error between the experiments and the model for the double bend case) value of 0.3 N/mm^2 is chosen for the stiffness of the elastic foundation.

Needle deflection is predicted for Case VI using both the kinematics-based and mechanics-based models. The resulting needle deflections in the xy -plane and xz -plane are shown in Fig. 14(e) and (f), respectively. The errors for the predicted needle shapes are provided in Table III. The maximum errors for the kinematics-based model are larger than the errors for the mechanics-based model: 2.20 and 3.77 mm, and 1.72 and 2.20 mm for deflections in the xy -plane and the xz -plane, respectively. This could be attributed to the assumption that the cut angle and radius of curvature are constant throughout insertion. In Fig. 14(f), we observe that after needle rotation the kinematics-based model assumes the needle continues in the same direction. The mechanics-based model accounts for tissue

TABLE III

ERRORS IN THE RECONSTRUCTED NEEDLE SHAPE USING FIBER BRAGG GRATING (FBG) SENSORS, AND PREDICTED NEEDLE SHAPE USING THE KINEMATICS-BASED (KB) AND MECHANICS-BASED (MB) MODELS FOR INSERTIONS IN THE GELATINE PHANTOM (CASES IV–VI)

Case	Plane	ϵ_s (mm)	$\epsilon_{s,\max}$ (mm)	ϵ_t (mm)
IV	FBG	xy	0.36 (0.03)	0.57 (0.02)
V	FBG	xy	0.20 (0.03)	0.53 (0.04)
VI	FBG	xy	0.18 (0.06)	0.47 (0.09)
		xz	0.33 (0.03)	0.74 (0.05)
VI	KB	xy	0.88 (0.06)	2.20 (0.30)
		xz	1.19 (0.23)	3.77 (0.58)
VI	MB	xy	0.28 (0.09)	1.72 (0.32)
		xz	0.53 (0.23)	2.20 (0.62)
				0.71 (0.53)

Experimental deflections from the camera images are used as reference. Mean values and standard deviations (in brackets) are provided. Overall error (ϵ_s), maximum error $\epsilon_{s,\max}$, and tip error (ϵ_t) are evaluated. Each experimental case is repeated three times.

relaxation (via the elastic foundation) and hence, this results in a change in slope when continuing insertion. The large error in predicted deflection using the kinematics-based model may be explained by the fact that the radius of curvature is not constant when bending out of plane.

VI. DISCUSSION

A prototype of a Nitinol needle with an integrated array of 12 FBG sensors is introduced in this study. These sensors are used to measure axial strain at several locations along the needle shaft, and this is used to calculate needle curvature. The 3-D needle shape is reconstructed from needle curvature. In this study, needle curvature is determined at four discrete locations using four sets of FBG sensors, consisting of three sensors each. Thus, a limited number of measurement points enables us to accurately approximate needle curvature for simple bending cases (i.e., single bend). For cases with multiple bend deflections, more FBG sensors are required in order to better approximate needle curvature. Linear spline interpolation of the measured curvatures using FBG sensors proved to be effective for single bend and double bend planar cases. However, for more complex bends (i.e., out-of-plane cases), we observed larger discrepancies between the reconstructed needle shape and deflection measured using camera images. These errors could be attributed to the limited number of FBG sensors and usage of a linear spline interpolation technique.

This study demonstrates the feasibility of using FBG sensors to accurately reconstruct the shape of the needle in a soft tissue. Information about needle shape during a surgical intervention (e.g., biopsy) can be used in algorithms for robotically steering flexible needles. Besides feedback about the current needle shape, such algorithms could benefit from models which provide information about the future needle path. Therefore, kinematics-based and mechanics-based models are presented in this study which predict the 3-D needle path for a flexible needle with an asymmetric (bevel) tip during insertion into a soft tissue. The mechanics-based model has shown to predict the needle shape more accurately for the out-of-plane insertion case than the kinematics-based model. However, the kinematics-based model is preferred, since it is easier to implement in a real-time con-

trol system for needle steering. In order to predict the needle shape using the kinematics-based model, more investigation is required about the radius of curvature and cut angle when the needle bends out of plane.

A. Conclusion

The needle shape is reconstructed for deflections applied in a free space, both for in-plane and out-of-plane needle deflection. Maximum errors for reconstruction in the free space are 0.20 mm (in-plane deflection with single bend), 0.51 mm (in-plane deflection with double bend), and 1.66 mm (out-of-plane deflection). Experiments are also performed in which the needle is inserted into a gelatine phantom (both in-plane and out-of-plane deflections). Reconstructed needle shapes are compared to experimental deflections using camera images. Maximum error in deflection for reconstruction using FBG sensors is 0.74 mm. These errors are comparable to results obtained in earlier studies where the shape of a surgical needle was reconstructed using FBG sensors [7], [8]. However, those studies did not consider out-of-plane needle deflection nor did they insert the needle into a soft-tissue simulant.

We have also presented 3-D kinematics-based and mechanics-based models for predicting needle deflection. Model parameters are fitted using in-plane experimental data. The models are validated using camera images as reference, but are also compared to results from FBG sensors. The kinematics-based model has a maximum error of 3.77 mm in predicted needle shape. The mechanics-based model shows closer agreement with experimental deflection: a maximum error of 2.20 mm is observed.

B. Future Work

We will investigate fabricating a prototype with more than four sets of FBG sensors which enables us to measure curvature at more locations along the needle shaft. We will also explore other interpolation methods for complex, out-of-plane, bending cases. In the current study, uncertainties introduced during the needle fabrication process (e.g., the effect of glue and optical fibers on the strain distribution) were neglected. These could also affect the reconstructed shape and hence, should be investigated in future studies.

As part of ongoing work, using the presented needle shape reconstruction technique, Abayazid *et al.* used the output from the FBG sensors in real time to steer the needle in 3-D space to a target in a soft-tissue simulant [21]. In the future, real-time reconstruction of needle shape using FBG sensors needs to be combined with the deflection models to enable accurate robotic needle steering in both soft-tissue simulates and biological tissue. Further, for accurate shape reconstruction, data from FBG sensors can also be coupled to a clinical imaging modality (such as ultrasound images) in order to track the needle and also motion of the target during insertion.

REFERENCES

- [1] S. Patil and R. Alterovitz, "Interactive motion planning for steerable needles in 3-D environments with obstacles," in *Proc. IEEE/EMBS Int. Conf. Biomed. Robot. Biomechatron.*, Tokyo, Japan, Sep. 2010, pp. 893–899.

- [2] N. Abolhassani, R. V. Patel, and M. Moallem, "Needle insertion into soft tissue: A survey," *Med. Eng. Phys.*, vol. 29, no. 4, pp. 413–431, 2007.
- [3] Z. Lunwei, Q. Jinwu, S. Linyong, and Z. Yanan, "FBG sensor devices for spatial shape detection of intelligent colonoscope," in *Proc. IEEE Int. Conf. Robot. Autom.*, New Orleans, LA, USA, Apr./May 2004, pp. 834–840.
- [4] L. Zhang, J. Qian, Y. Zhang, and L. Shen, "On SDM/WDM FBG sensor net for shape detection of endoscope," in *Proc. IEEE Int. Conf. Robot. Autom.*, Barcelona, Spain, Apr. 2005, pp. 1986–1991.
- [5] X. Yi, J. Qian, L. Shen, Y. Zhang, and Z. Zhang, "An innovative 3-D colonoscope shape sensing sensor based on FBG sensor array," in *Proc. IEEE Int. Conf. Inf. Acquisit.*, Jeju Island, Korea, Jul. 2007, pp. 227–232.
- [6] I. Payo, V. Feliu, and O. D. Cortázar, "Fibre Bragg grating (FBG) sensor system for highly flexible single-link robots," *Sens. Actuators A, Phys.*, vol. 150, no. 1, pp. 24–39, 2009.
- [7] Y. L. Park, S. Elayaperumal, B. Daniel, S. C. Ryu, M. Shin, J. Savall, R. Black, B. Moslehi, and M. Cutkosky, "Real-time estimation of 3-D needle shape and deflection for MRI-guided interventions," *IEEE/ASME Trans. Mechatronics*, vol. 15, no. 6, pp. 906–915, Dec. 2010.
- [8] K. Henken, D. van Gerwen, J. Dankelman, and J. J. van den Dobbelaer, "Accuracy of needle position measurements using fiber Bragg gratings," *Minimally Invas. Therapy Allied Technol.*, vol. 21, no. 6, pp. 408–414, 2012.
- [9] V. Mishra, N. Singh, U. Tiwari, and P. Kapur, "Fiber grating sensors in medicine: Current and emerging applications," *Sens. Actuators A, Phys.*, vol. 167, no. 2, pp. 279–290, 2011.
- [10] O. Hill and G. Meltz, "Fiber Bragg grating technology fundamentals and overview," *J. Lightw. Technol.*, vol. 15, pp. 1263–1276, Aug. 1997.
- [11] S. Misra, K. B. Reed, B. W. Schafer, K. T. Ramesh, and A. M. Okamura, "Mechanics of flexible needles robotically steered through soft tissue," *Int. J. Robot. Res.*, vol. 29, no. 13, pp. 1640–1660, 2010.
- [12] R. J. Roesthuis, M. Abayazid, and S. Misra, "Mechanics-based model for predicting in-plane needle selection with multiple bends," in *Proc. IEEE/EMBS Int. Conf. Biomed. Robot. Biomechatron.*, Rome, Italy, Jun. 2012, pp. 69–74.
- [13] R. J. Webster, J. S. Kim, N. J. Cowan, G. S. Chirikjian, and A. M. Okamura, "Nonholonomic modeling of needle steering," *Int. J. Robot. Res.*, vol. 25, no. 5–6, pp. 509–525, 2006.
- [14] V. Duindam, R. Alterovitz, S. Sastry, and K. Goldberg, "Screw-based motion planning for bevel-tip flexible needles in 3-D environments with obstacles," in *Proc. IEEE Int. Conf. Robot. Autom.*, Pasadena, CA, USA, May 2008, pp. 2483–2488.
- [15] R. J. Roesthuis, Y. R. van Veen, A. Jahya, and S. Misra, "Mechanics of needle-tissue interaction," in *Proc. IEEE Int. Conf. Intell. Robot. Syst.*, San Francisco, CA, USA, Sep. 2011, pp. 2557–2563.
- [16] O. Bauchau and J. Craig, *Structural Analysis*. New York, NY, USA: Springer-Verlag, 2009.
- [17] J. Gere and S. Timoshenko, *Mechanics of Materials*. Cheltenham, U.K.: Stanley Thornes, 1999.
- [18] A. Othonos, K. Kalli, D. Pureaur, and A. Mugnier, "Fibre Bragg gratings," in *Optical Sciences*. New York, NY, USA: Springer-Verlag, 2006, pp. 189–262.
- [19] A. Gefen and B. Dilmoney, "Mechanics of the normal woman's breast," *Technol. Health Care*, vol. 15, no. 4, pp. 259–271, 2007.
- [20] A. Jahya, F. van der Heijden, and S. Misra, "Observations of three-dimensional needle deflection during insertion into soft tissue," in *Proc. IEEE/EMBS Int. Conf. Biomed. Robot. Biomechatron.*, Rome, Italy, Jun. 2012, pp. 1205–1210.
- [21] M. Abayazid, M. Kemp, and S. Misra, "3-D flexible needle steering in soft-tissue phantoms using fiber Bragg grating sensors," in *Proc. IEEE Int. Conf. Robot. Autom. (ICRA)*, Karlsruhe, Germany, May 2013, pp. 5823–5829.



Roy J. Roesthuis (S'11) received the B.Sc. degree in electrical engineering and the M.Sc. degree in mechatronics, both from the University of Twente, Enschede, The Netherlands, in 2009 and 2011, respectively, where he is currently working toward the Doctoral degree in the Robotics and Mechatronics Group.

His research interests include robotics for medical procedures.



Marco Kemp received the B.Sc. degree in electrical engineering and the M.Sc. degree in mechatronics from the University of Twente, Enschede, The Netherlands, in 2010 and 2012, respectively. He worked on his M.Sc. degree project within the Robotics and Mechatronics Group, which focused on steering a flexible needle using fiber Bragg grating sensors.

He is currently a Mechatronic Designer at Océ Technologies B.V. (Canon Group), Venlo, The Netherlands.



John J. van den Dobbelaer received the M.Sc. degree in experimental psychology from the University of Groningen, Groningen, The Netherlands, in 1998, and the Ph.D. degree from the Department of Neuroscience, Erasmus MC, Rotterdam, The Netherlands, for his research into human motor control, motor learning, and sensorimotor integration.

In 2005, he became a Research Fellow with the Department of Biomechanical Engineering, Delft University of Technology, Delft, The Netherlands, where he has been an Assistant Professor in the research group Minimally Invasive Surgery and Interventional Techniques (MISIT) since 2007. His research projects focus on the study of instrument-tissue interaction and the development of new instruments for minimally invasive interventions.



Sarthak Misra (S'05–M'10) received the master's degree in mechanical engineering from McGill University, Montreal, QC, Canada, and the doctoral degree in mechanical engineering from The Johns Hopkins University, Baltimore, MD, USA.

He is currently an Associate Professor (Robotics and Mechatronics) and affiliated with MIRA—Institute for Biomedical Technology and Technical Medicine, University of Twente, Enschede, The Netherlands. Prior to commencing his studies at Johns Hopkins, he worked for three years as a dynamics and controls analyst on the International Space Station Program. His research interests include biomechanics and robotics.

Dr. Misra received a 2010 Netherlands Organization for Scientific Research (NWO) VENI Award. He is an Associate Editor of the IEEE Robotics and Automation Society Conference Editorial Board.